JOURNAL OF PROPULSION AND POWER
Vol. 24, No. 4, July–August 2008

Unsteady Strong Shock Interactions in a Transonic Turbine: Experimental and Numerical Analysis

Guillermo Paniagua,* Tolga Yasa,† and Andres de la Loma‡
von Kármán Institute,
1640 Rhode Saint Genese, Belgium
Lionel Castillon§
ONERA, 92322 Châtillon, France
and
Thomas Coton¶
Société Nationale d'Etude et de Construction de Moteurs d'Aviation,
77550 Moissy Cramayel, France

DOI: 10.2514/1.34774

The aerothermal performance of highly loaded high-pressure turbines is abated by the unsteady impact of the vane shocks on the rotor. This paper presents a detailed physical analysis of the stator–rotor interaction in a state-of-the-art transonic turbine stage at three pressure ratios. The experimental characterization of the steady and unsteady flowfield was performed in a compression tube test rig. The calculations were performed using ONERA's code elsA. This original comparison leads to an improved understanding of the complex unsteady flow physics of a high-pressure turbine stage. The vane shock impingement on the rotor originates a separation bubble on the rotor crown that is responsible for the generation of high losses. A model based on rothalpy conservation has been used to assess the pressure loss. The analysis of the unsteady forcing relates the shock patterns with the force fluctuations.

Nomenclature

H	=	turbine span height, m
M_{is}	=	isentropic Mach number
Nu	=	Nusselt number
P	=	pressure, Pa
S	=	curvilinear abscissa along wall surface, m
T	=	temperature, K
T_r	=	rotor passing period, s
T_{rotation}	=	wheel rotation period, s
T_s	=	stator passing period, s
t	=	time, s
x	=	turbine axial direction, m
y	=	turbine radial direction, m
y^+	=	normalized distance of first wall cell

Subscripts

w	=	wall
s	=	static
0	=	freestream, total conditions
1	=	stator inlet
2	=	stator–rotor interface
3	=	rotor outlet

Presented as Paper 1218 at the 18th International Symposium on Airbreathing Engines, Beijing, China, 2–7 September 2007; received 25 September 2007; revision received 12 March 2008; accepted for publication 18 March 2008.

*Assistant Professor, Turbomachinery and Propulsion Department, Chaussée de Waterloo 72; paniagua@vki.ac.be. AIAA Member.

†Ph.D. Student, Turbomachinery and Propulsion Department, Chaussée de Waterloo 72.

‡Research Engineer, Turbomachinery and Propulsion Department, Chaussée de Waterloo 72.

§Senior Research Engineer, 29 Avenue de la Division Leclerc–BP72; Lionel.Castillon@onera.fr.

¶Design Engineer, Site de Villaroche, Rond-Point René Ravaud.

I. Introduction

IN HIGHLY loaded turbine stages, the nozzle guide vane (NGV) exit flow is often transonic. The design of efficient turbines thus requires a thorough understanding of the unsteady interactions effects on the pressure and heat transfer. In spite of the radical weight reduction offered by trans- or supersonic single stages, their choice is handicapped by the large forcing and lower performance caused by the NGV trailing-edge (TE) shocks. These complex vane shock patterns are dictated by the vane geometry and fluctuate at the rotor blade passing frequency due to the rotor blockage.

Upstream potential field effects, vane trailing-edge shocks, and vane wakes on the rotor flowfield have been studied by various research groups (Korakianitis [1], Miller et al. [2], Hilditch et al. [3]). Giles [4] observed that 40% of the variation of the rotor blade lift is produced by the strong shocks in a single-stage turbine. Laumert et al. [5] investigated numerically the source of blade excitation mechanisms present in a subsonic, transonic, and supersonic vane. The results show that at high vane exit Mach numbers, the dominating excitation source is the vane trailing-edge shock system, and the amplitude of the force and torque increases with increasing stator exit Mach number. Dénos et al. [6] studied the blade row interactions experimentally and numerically at the blade midspan, with time-resolved variations in relative total pressure around 40% of the mean level. The propagation effect of shock waves on turbine blades has already been the subject of experimental and numerical studies. The first experimental studies on the subject concern linear cascade investigations. Graham and Kost [7] performed steady flow investigations on the shock—boundary-layer interaction in a high turning transonic turbine cascade with the help of schlieren flow visualization. Johnson et al. [8,9] introduced unsteady effects using an upstream rotating bar system to simulate the shock wave and the wake passing. They proposed a model to explain the heat transfer fluctuations on the rotor blade associated with the impingement of the NGV trailing-edge shock waves. Dunn et al. [10], followed by Abhari et al. [11], have performed time-averaged and time-resolved

measurements of a transonic single-stage research turbine in a short duration facility. More recently, Popp et al. [12] and Nix et al. [13,14] reported the progression effect of shock waves on film-cooled blades through a transonic turbine linear cascade.

Concerning numerical simulations, the first transonic turbine stage calculations were quasi-three-dimensional, as those performed by Rao and Delaney [15] on Bennett's investigations, and by Giles on the experiments of Abhari et al. [11]. Afterward, the progress in computational performance made three-dimensional computations affordable, as the transonic turbine stage simulation performed by Saxer and Felici [16]. These calculations have enabled researchers to highlight the complexity of the unsteady shock physics in a transonic turbine environment.

In the current paper, the steady and unsteady flowfields in the vane and rotor blade are analyzed in detail using pressure and heat transfer measurements together with accurate computational fluid dynamics (CFD) calculations. The steady and unsteady forces acting on the rotor disk are computed and studied for different operating conditions.

II. Generalities

A. Turbine Stage

The turbine stage is composed of uncooled cylindrical vanes and uncooled rotor leaned blades. The design characteristics of both the vane and rotor are summarized in Table 1. The current turbine stage is 2 deg more staggered than the turbine stage recently studied by Dénos et al. [6]. Sieverding et al. [17] published the coordinates of the former cooled cylindrical vane; the coordinates of the rotor are, however, proprietary.

B. Test Conditions

The measurement campaign included tests at vane exit Mach numbers 1.07 and 1.25, the rotor outlet Mach numbers ranging from 0.65 to 1.18. The operating conditions comprised three pressure ratios ($P_{01}/P_{s3} = 5.1,\ 3.8,\ 2.4$) at a fixed Reynolds number (1.1×10^6). At the turbine inlet, plane 1 is situated $0.724 \times C_{s,\mathrm{ax}}$ upstream of the vane leading edge. Plane 2, downstream of the vane, stands $0.043 \times C_{s,\mathrm{ax}}$ downstream of the vane trailing edge. Plane 3 is located at the turbine stage outlet, in particular $0.45 \times C_{r,\mathrm{ax}}$ downstream of the rotor trailing edge. Figure 1a depicts the three measurement planes in a meridional view of the turbine.

Table 2 lists the operating conditions, including the degree of reaction

$$r = 1 - \frac{1 - (P_{s2}/P_{01})^{\gamma-1/\gamma}}{1 - (P_{s3}/P_{01})^{\gamma-1/\gamma}}$$

stage loading, and flow coefficient. The stage inlet conditions are identical for all tests ($P_{01} = 1.65$ bar, $T_{01} = 434$ K, $M_1 = 0.14$, and

Table 1 Vane and rotor design characteristics at midspan

	Vane	Rotor
Number of airfoils	43	64
Axial chord, C_{ax}, mm	41.16	39.78
aspect ratio, C_{ax}/h	0.812	0.738
$R_{\mathrm{hub}}/R_{\mathrm{tip}}$	0.872	0.864
Stagger, deg	54	32
Pitch/C_{ax}	1.313	0.912
Throat/pitch	0.245	0.401

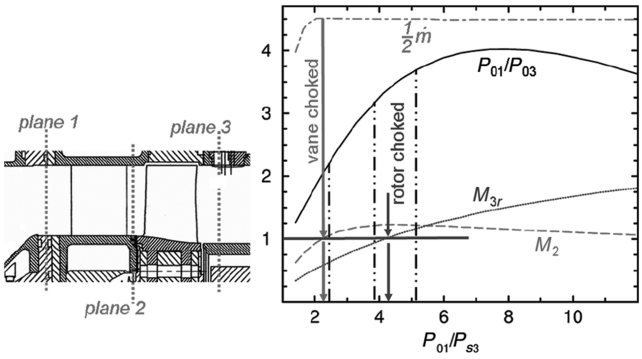

a) b)

Fig. 1 Turbine operating conditions: a) axial position of the measurement planes, b) Mach numbers and mass-flow across the turbine stage in function of the pressure ratio.

$Tu \sim 5\%$, Yasa et al [18]). The selected rotational speed was 6500 rpm, i.e., 108.3 rev/s, resulting in vane and blade passing frequencies of 4.7 and 6.9 kHz, respectively. Tests were performed with an axial distance between the NGV trailing edge and rotor leading edge equal to 40% of the vane axial chord, and a corrected speed $\mathrm{rpm}/\sqrt{T_{01}} = 311$.

Figure 1b presents the results of a nonisentropic-radial-equilibrium calculation. The turbine mass flow remains constant above a pressure ratio $P_{01}/P_{s3} \sim 2.3$, when the vane becomes choked. The maximum vane exit Mach number ($\sim$1.25) is obtained when the rotor is choked at $P_{01}/P_{s3} \sim 4.2$; above this pressure ratio, the vane exit Mach number decreases slightly due to shock losses. At total-to-static pressure ratios above eight, the total-to-total pressure ratio decays, due to enormous pressure losses in the rotor.

III. Experimental Apparatus

A. Turbine Test Rig

The experiments were executed in the von Kármán Institute turbine compression tube facility (Sieverding and Arts [19]). This short duration facility is able to simulate the aerothermal performance of highly loaded high-pressure turbines in a larger scale, by reproducing the temperature ratios, Reynolds numbers, and Mach numbers of the actual engine conditions. The facility comprises a cylinder where air is compressed by a free piston, the test section, and a large tank at vacuum where the gas is vented. Pressure and temperature levels are kept constant by adjusting the piston backpressure and the turbine mass flow. Further details on the operation cycle are provided by Dénos and Paniagua [20].

B. Measurement Techniques

In the absolute frame, pressure and temperature were measured at three measurement planes corresponding to three locations along the turbine axis. Radial traverses of pressure and temperature are performed in planes 1 and 3. The transient operating mode of the facility allows investigating the external convective heat transfer based on wall temperature measurements. Three different vanes have been instrumented at midspan with a total of 39 platinum thin-film gauges. The gauges are deposited on an Upilex sheet, which is wrapped around the airfoils, made of Plexiglas (double-layered system), as displayed in Fig. 2a. On the rotor, six blades were instrumented at midspan with 24 Macor-based gauges (single-layered system). The thermal properties of the different substrates, Upilex, Plexiglas, and Macor, have been obtained in a

Table 2 Operating conditions

Condition	P_{01}/P_{s3}	Re_c	$M_{2,\mathrm{is}}$	$M_{3r,\mathrm{is}}$	r	$\Delta H/U^2$	V_{ax}/U
Low	2.42	1.06×10^6	1.071	0.65	0.15	1.28	0.48
Nom	3.86	1.07×10^6	1.242	0.97	0.27	1.86	0.62
High	5.12	1.07×10^6	1.249	1.18	0.37	2.02	0.70

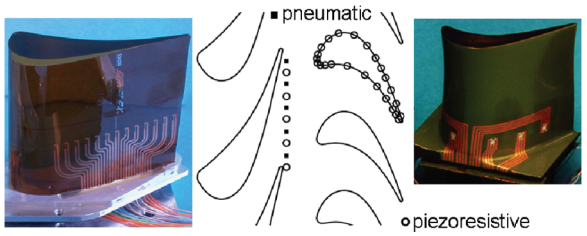

a) b) c)

Fig. 2 Turbine instrumentation: a) thin-film gauges in the stator, b) pressure gauges location in plane 2, and c) piezoresistive gauges in the rotor.

freejet facility, with known heat flux, using an optimization routine (Billiard et al. [21]).

In plane 2, the pitchwise distribution of static pressure is measured with 10 pneumatic and 10 subsurface-mounted piezoresistive pressure transducers placed at the hub and casing endwall, as depicted in Fig. 2b. Additionally, rotor blades instrumented with 72 flush-mounted piezoresistive sensors allow one to measure the steady and unsteady rotor static pressure at three different span heights: 15, 50, and 85% (Fig. 2c). Based on repeatability analysis, the accuracy is estimated to be ± 3 mbar for the pneumatic taps and ± 15 mbar for the fast response transducers, with a 95% of confidence.

Piezoresistive pressure transducers are also sensitive to temperature variations and centrifugal forces. During a typical test, the rotor is submitted to a temperature transient from 300 K to about 380 K in less than 100 ms. Thus, conventional temperature compensation units are not suitable for this application. Specific calibration tests were performed, monitoring the pressure and temperature sensitivity of the gauge, while the exact pressure variation is measured with accurate pneumatic lines. This calibration procedure, together with the compensation procedure for both temperature and centrifugal forces, is fully described by Dénos [22].

The raw data were acquired at two different sampling frequencies. The steady part of the measurements is low-pass filtered (750 Hz) and sampled at 1.5 kHz. The unsteady part of the data is high-pass filtered at 100 Hz, and amplified by 10, to increase measurement resolution. Then, the signal is sampled at 300 kHz.

The phase-locked averaging (PLA) technique is used to analyze the unsteady data. This routine classifies the raw signal in a minimum of 40 classes and reports one vane or rotor passing event without any interpolation. The mean and root mean square (rms) of each class are computed, producing the so-called phase-locked average as well as the random unsteadiness. A full rotor revolution is used, because the mean acceleration is $\sim$83.7 rad/s, the resulting variation of the rotational speed is only 7 rpm. The technique allows discriminating the nondeterministic (rms) and deterministic (PLA) part, such as blade/vane passing of the signal.

IV. Numerical Tools

To highlight the shock physics across the stage, three-dimensional computations have been carried out by ONERA with its in-house code elsA [23]. This CFD code solves the 3-D–RANS (Reynolds-averaged Navier–Stokes) equations with a finite volume method based on a multidomain approach on structured grids. The computational domain, composed of one blade per row, is meshed with a 12-block structured grid, including 3.10^6 points. "O-blocks" are used around the blades, and "H-blocks" fill the rest of the passage, as shown on Fig. 3a. The rotor tip clearance gap is also taken into account. The values of y^+ at the blade wall is between $1 \sim 2$. Concerning the turbulence modeling, Menter's k-ω model [24] was used with the help of Arnal's transition model [25] on the stator.

Boundary conditions based on the characteristics method are prescribed at the stage inlet and outlet. The stage pressure ratio is specified at the hub outlet, and then radial equilibrium is applied. Walls are treated applying a nonslip condition associated with a uniform temperature distribution ($T_w = 289$ K). The unsteadiness

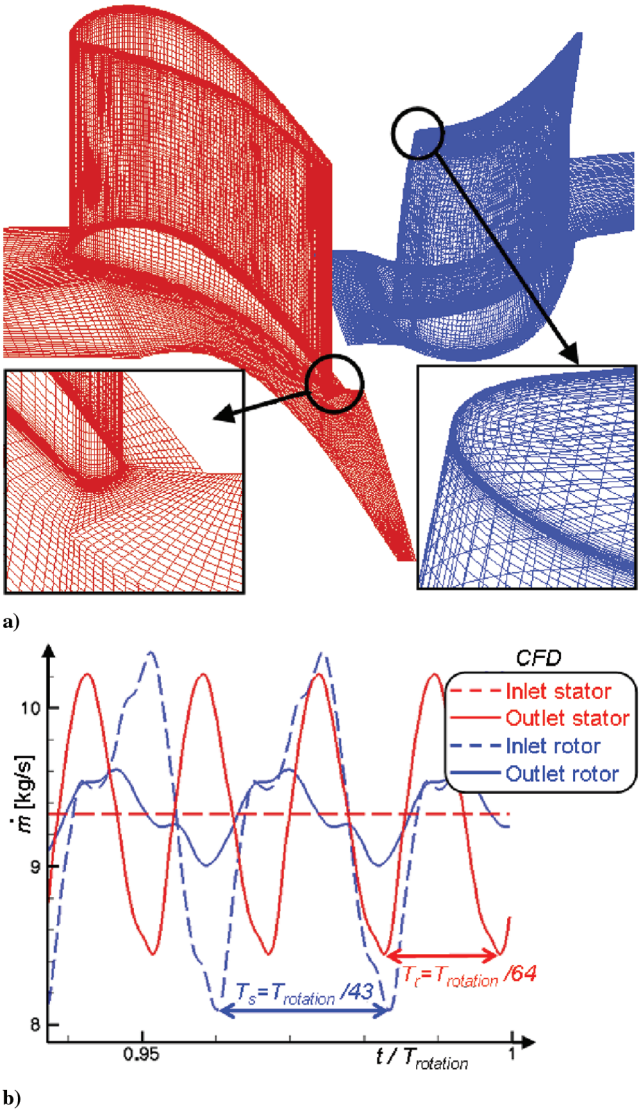

Fig. 3 Description of elsA: a) 3-D view of the grid, b) mass-flow time evolution.

induced by the blade passing is taken into account through the use of phase-lagged conditions, both at the interface and on periodic boundaries. Erdos and Alzner [26] were among the first to take advantage of the phase-lagged properties for turbomachinery computations. This method, implemented in elsA [27,28], consists in storing the Fourier transform of the flow variables at both the time-periodic boundaries and the stator–rotor interface to deal with the phase lag existing between adjacent passages. Accordingly, the computational domain is limited to a single blade passage for each row, being the periodic borders of the mesh matching. This technique gives a fundamental advantage, as no assumption is made concerning the blade number ratio, nor the geometry of the blade. The unsteady effects are only linked to the blade passing frequencies.

Concerning the convergence of the calculations, one rotation of the whole wheel is covered in 27,520 time steps (430 times steps for one rotor passing period) and takes 25 CPU hours on ONERA's vector supercomputer NEC-SX8$^+$, the code operating at 1.0 μs/iterations/grid points. Figure represents the time evolutions of the mass flow provided in four axial planes. The mass flow upstream of the NGV is constant as the stator flow is choked and no unsteadiness propagates upstream of the vane throat. At the interface, the time-resolved mass flow in the absolute frame of reference evolves with the rotor passing period, while it is governed by the stator passing period in the rotating frame.

Once the periodic convergence is reached, reconstruction of the flowfield within the stage is achieved to check the satisfactory

convergence of the computation with a good continuity of the flow variables both at the time-periodic boundaries and at the interface.

V. Turbine Flowfield Analysis

A. Shock Propagations in the Stage

Figure 4 displays shock sketches and normalized density gradients at 25% of the span height, at high-pressure ratio (henceforth, "high" indicates high-pressure ratio configuration). The four snapshots reveal a complex shock system: the NGV trailing-edge shocks interact periodically both with the wakes and with the adjacent blades, generating repeated reflections. At any moment, different shock waves are moving through the stage, some upstream, other downstream, while changing intensity. The rotor blade passing in front of the vane channel produces a blockage effect, and instantaneous convergent/divergent nozzles [6]. The TE shock wave moves accordingly to match the new instantaneous pressure ratio, becoming less inclined. This effect produces a small up-and-down motion of the shock. The following analysis confirms some observations made in previous experimental and numerical studies [9,11,13].

At $t/T_r = 0$, when the leading edge of S_1 and R_1 are aligned, the direct shock A of S_0 hits the crown of R_1 on the suction side, whereas the right-running shock B of S_0 which strikes the adjacent stator on the suction side is weakly reflected. The impact on the rotor of the left-running shock A generates a reflected shock wave C which travels upstream across the passage toward the pressure side of the adjacent blade. The rotor left-running trailing-edge shock D is rather weak at this instant, and the shock does not reach the neighboring blade suction side. At $t/T_r = 0.25$ the left-running shock A has completed the sweeping of the rotor crown; it has diffused and lost strength. Simultaneously, the reflected right-running shock B strengthened. As this reflected shock crosses the wake, it bends to accommodate the low-speed flow inside the wake. Because of this bending, a new shock wave is created which is reflected back toward the vane. By contrast, the reflected shock C continues its movement upstream.

In engine practice, the NGV boundary layer is completely turbulent, and sometimes relaminarization takes place around the suction side high-curvature region, followed by transition to turbulent flow again. In this work, the vane suction side boundary layer presents a laminar behavior. In high-speed flows, shocks introduce major changes in the boundary layer, resulting in complex mutual interaction between the boundary layer and the freestream. The interaction region extends over a considerable distance along the streamwise direction. The strength of the reflected shock depends upon whether or not a separation zone appears. If it does, the upstream boundary-layer curvature is greater, and the reflected shock is strengthened. The unsteady nature of the separation bubble created by the direct shock, oscillating up and down at the blade passing frequency, produces a reflected shock with varying intensity depending on the actual size of the separated region.

The shock waves approaching the rotor bend as they reach the vicinity of the rotor surface. The bending of the shocks has to do with the velocity of the flow and the backpressure of the shock. If there is a strong backpressure, the shock bends to accommodate this backpressure. This effect is more noticeable in the case of the reflected one (B at $t/T_r = 0.75$), where the shock is usually normal to the rotor surface (bottom of Fig. 4). The stronger direct shock is often oblique to the surface (A at $t/T_r = 0.0$ and 0.25). A normal shock impingement may create a separation bubble [29] depending on the strength of the interaction, but no reflected shock is produced. These two different interaction mechanisms are outlined in Fig. 4 at the bottom.

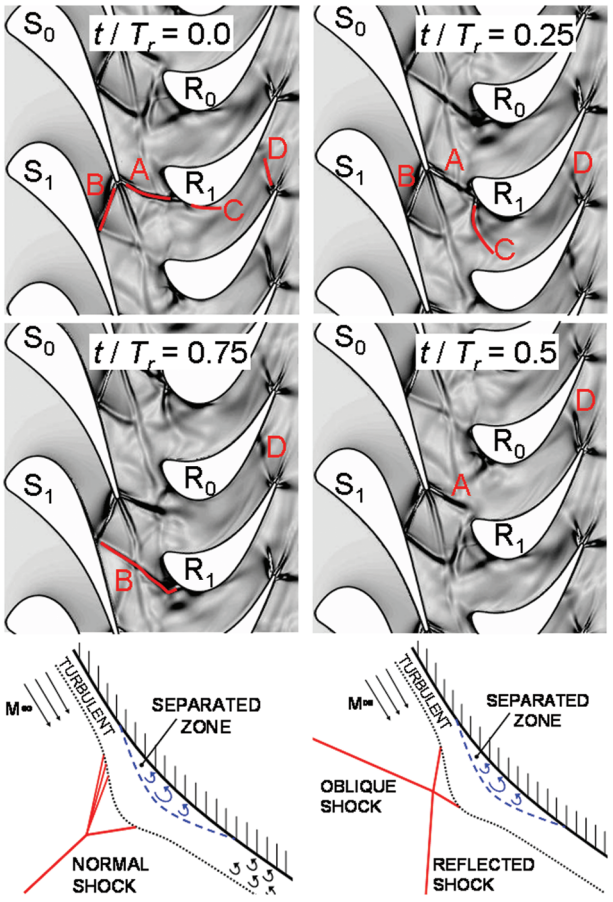

Fig. 4 Top: Shock progression through the stage: schematic (left) and density gradient (right); at high-pressure ratio $y/H \sim 25\%$. Bottom: Different shock–boundary-layer interactions.

B. Interstage Flowfield

Figure 5 represents the pitchwise pressure distribution at the tip and hub at the interface (plane 2). On the tip, the decrease of pressure from pressure to suction side followed by the right-running shock is well reproduced by the calculation. The discrepancies observed around pitch value ~0.7 are probably linked to endwall secondary flows located on the suction side corner. The pressure distributions for the nominal- and high-pressure ratio configurations are identical as the exit Mach number is the same. (Henceforth, "nom" indicates nominal pressure ratio configuration). At the hub, the pressure distribution differs from the tip pattern owing to the stronger reflected

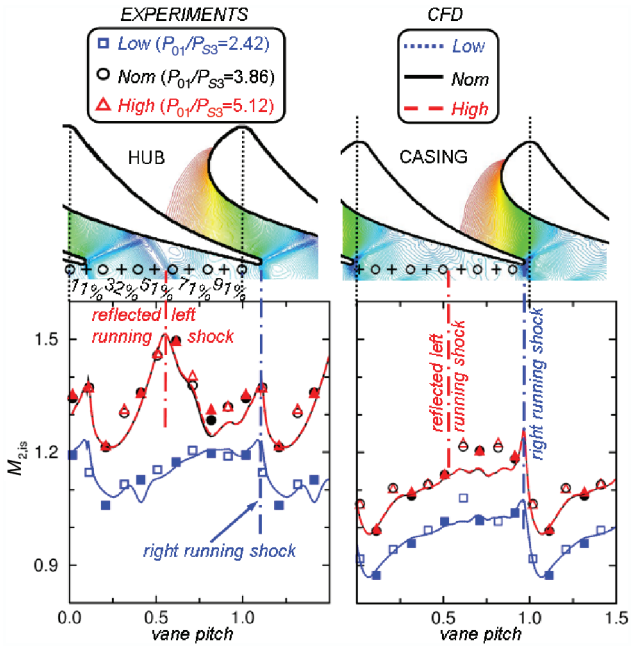

Fig. 5 Pitchwise pressure distribution at the vane exit endwalls, plane 2. Left: at hub; Right: at tip.

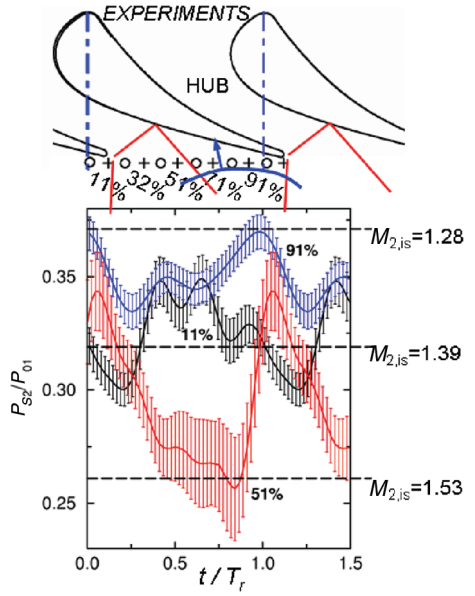

Fig. 6 Unsteady static pressure at the vane exit for the nom-pressure ratio at hub.

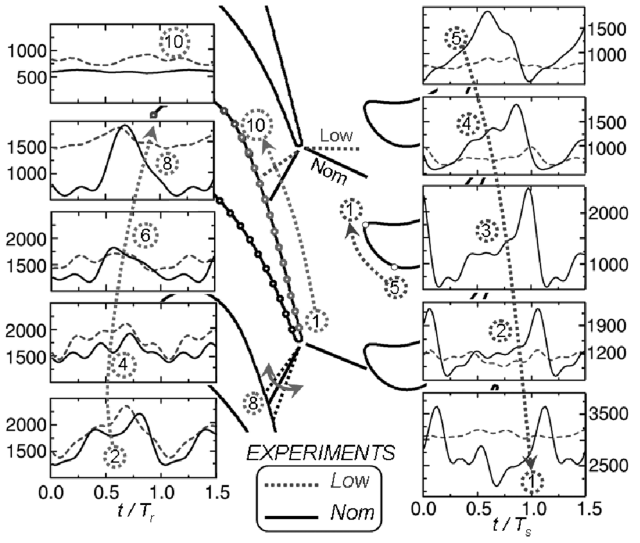

Fig. 7 Heat transfer in the interstage region.

left-running shock B. Because the CFD agrees well with the experiments, we can conclude that the CFD accurately models the physics.

Figure 6 represents the unsteady pressure at the hub at nom pressure ratio. The data are decomposed into the deterministic (or time resolved, or periodic) and random (or time unresolved). The solid lines represent the deterministic component (or mean unsteady signal), which was obtained using the phase-locked-averaging technique at the blade passing frequency. The vertical bars represent the range of variation of the random component, which corresponds to the ±rms, at each rotor position, i.e., the range of dispersion of the raw unsteady signal with a confidence level of 68%. The location of each sensor is shown on the graphs, in terms of the percentage of vane pitch. Shocks are recognized by a minimum in pressure followed by a sudden augmentation. The sensor located at 51% experiences the largest pressure fluctuation during the rotor passage. A pressure minimum appears when the rotor attains $\Phi_{\text{rotor}} = 0.84$ ($M_{2\text{is}} \sim 1.53$); at that instant, an intense reflected left-running vane trailing-edge shock flaps across the sensor. During $\Phi_{\text{rotor}} = 0.4$–$0.7$, the high levels of rms should be attributed to the passage of turbulent structures (random), vane wakes, and the secondary flows. These turbulent patterns change in direction depending on the rotor blockage.

Both sensors located at 11 and 91% of the vane pitch exhibit a similar pattern in rotor phase. For the 11% sensor, the rise in pressure occurring at $\Phi_{\text{rotor}} = 0.25$ ought to be due to the flapping of the right-running shock, due to the local rotor blockage. Simultaneously, the sensor located at 91% undergoes a pressurization that should be due to the rotor reflected shock C (Fig. 4). The highest rms values are reached around $\Phi_{\text{rotor}} = 0.5$ for both sensors. At the tip, the random component of the unsteadiness is at least two to three times smaller than at the hub.

Figure 7 shows the time-resolved, plus the steady Nusselt number, for selected gauges at midspan on the vane and rotor blades at nom- and low-pressure ratios ("low" indicates low-pressure ratio configuration). The largest heat transfer fluctuations are confined to the vane rear suction side and rotor crown. The vane pressure side and front suction side are geometrically hidden from the rotor, besides, the vane trailing-edge shocks prevent major fluctuations from traveling upstream. Whereas the rotor crown is submitted periodically to the vane trailing-edge shocks and wakes, the vane rear suction side flowfield is dominated by shock waves reflected by the rotor and the rotor potential field. A strong fluctuation travels upstream on the rotor crown, from gauge 5 to 1, due to the direct shock A impingement (Fig. 4). This shock wave is reflected backward (shocks C in Fig. 4) reaching the upstream vane, hitting first close to the vane trailing edge and propagating thereafter upstream across the vane suction side. At nom, the vane highest fluctuation is encountered at gauge 8 due to the direct impact of the oscillating right-running TE shocks, causing a separated zone. The magnitude of this fluctuation is directly comparable to those present in the rotor. Upstream of the impingement (gauge 10), the fluctuations are lessened. The rotor has effectively a large influence on the vane rear suction side, which is directly exposed to the highly unsteady interstage flowfield. The reduction of the pressure ratio has a strong impact on the unsteady heat load across the stage, especially on the rotor blade where a notable net reduction is revealed from nom to low, due to weaker incoming shock waves.

C. Time-Averaged Results on the Vane and Rotor Blades

Figure 8 compares the isentropic Mach number distributions at midspan on both the vane and rotor blades for the three pressure ratios. Excellent agreement is obtained between the experimental and numerical data. The increase of the stage pressure ratio leads to an increase of the trailing-edge shock inclination, shifting the impact of the trailing-edge shock downstream. Moreover, the increase in pressure ratio raises the Mach numbers on the rear part of the vane suction side. On the vane, the Mach number distributions are

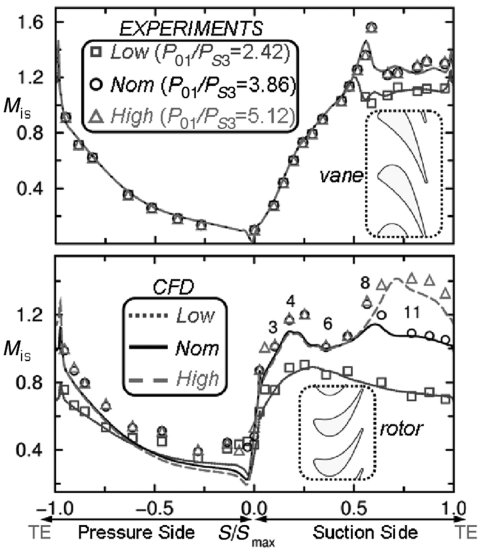

Fig. 8 Isentropic Mach number distribution on the NGV and rotor blade at midspan for the three pressure ratios.

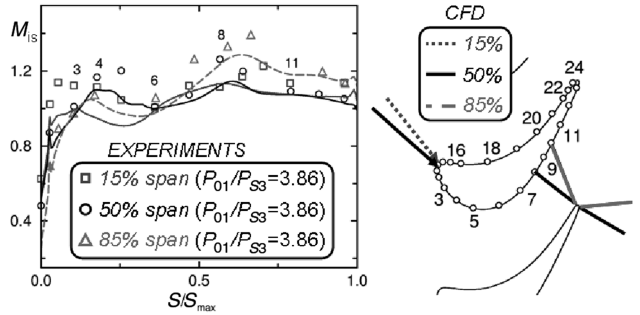

Fig. 9 Pressure distributions on the rotor suction side at three span heights for the nom-pressure ratio.

identical for the nom- and high-pressure ratios as the exit Mach number remains the same. The increase of the blade loading with the pressure ratio implies higher acceleration rates on the rear part of the suction side. For the nom- and high-pressure ratio, the rotor outlet Mach number is transonic and, therefore, one can notice the impact of the adjacent blade's left-running shock D at $S/S_{\max} \sim 0.6$ and 0.7, respectively.

Figure 9 shows the rotor suction side velocity distribution at 15% span, midspan, and 85% span for the nom condition. The discrepancy at 15% span has been attributed by Paniagua et al. [30] to the stator rim—rotor platform cavity flow ingestion, which has not been simulated in the current CFD study. At 15% span, there is more positive incidence than at midspan. The stagnation points move toward the pressure side resulting in a higher acceleration rate on the front suction side. Nevertheless, the CFD captures the actual trends. At 15% span, the left-running trailing-edge shock hits the rear suction side at gauge 10, instead of at gauge 8 at midspan. This is reasonable because the rotor exit flow is higher at the hub, hence the shocks are more oblique.

Figure 10 represents the Nusselt number distribution on the stator and rotor at midspan. In the vane, the highest heat flux levels are encountered in the stagnation region, due to the lack of insulation from the boundary layer. As the boundary layer gradually develops and thickens, the heat transfer decreases both on the pressure and suction side. Along the front pressure side, the flow is rapidly

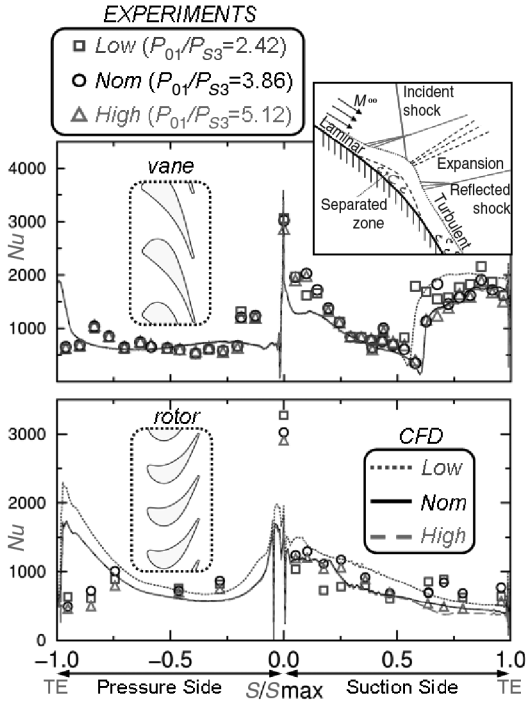

Fig. 10 Experimental and CFD Nusselt number distribution on the stator and rotor at midspan.

accelerated in the convex surface, resulting in a substantial decrease of the Nusselt number, up to a plateau of $Nu = 750$. This plateau indicates a laminar/transitional state of the boundary layer. On the suction side, the favorable pressure gradient and convex curvature accelerates continuously a laminar boundary layer until location $S/S_{\max} \sim 0.52$, for the low-pressure ratio, and location $S/S_{\max} \sim 0.58$ for the nom- and high-pressure ratios. At those locations, the sudden rise of heat transfer and static pressure is due to the impingement of the right-running trailing-edge shock from the neighboring vane. The time-averaged heat transfer levels in the vane rear suction side are higher at the low-pressure ratio because the transition onset occurs earlier upstream following the incident right-running shock.

On the blade, in the front region, the heat transfer rates depend on the local Reynolds number, the freestream turbulence, and degree of isotropy in the turbulent flow. The rotor boundary-layer status is transitional—turbulent as the heat transfer levels encountered follow in between those of a fully turbulent and laminar calculation. The principal difference between the response of turbulent (rotor) and laminar boundary layers (vane) to shock impingements is the greater ability of the former to withstand adverse pressure gradients without separating. When no separation takes place, the incident shock merely produces a thickening of the layer in the immediate vicinity of the impact point. However, if the incident shock is strong enough, the turbulent boundary layer might separate. The differences in the measurements are confined mainly to the suction side. At nom- and high-pressure ratios, the positive incidence ($\sim$14 deg) of the flow produces a stronger acceleration on the front suction side compared with the low condition ($\sim$8 deg). This acceleration rate is associated with a higher heat transfer level for nom/high in that part of the blade.

D. Steady Forcing on the Rotor

Figure 11 displays the unsteady static pressure carpet plots on the rotor surface at midspan, at low- and high-pressure ratio. The greatest pressure variation occurs around $t/T_s = 0.0$, corresponding to the passage of the direct vane TE shock A. In gauge 1, the pressure rises 10.5% of the average level for the low condition, whereas it amounts to 15.6% for the high case. However, the highest fluctuations are observed in the crown of the rotor blade in gauge 3: 27% of inlet total pressure.

The bottom of Fig. 11 examines the measured and computed pressure fluctuations on the rotor blade. It is possible to associate these pressure fluctuations with two major wave passing events. First of all, the sweeping on the crown of the rotor of the NGV left-running shock A is clearly evident. Gauges 5–15 are affected by this shock leading to a fast increase of pressure. The second phenomenon is the impingement of the trailing-edge right reflected shock B, which affects gauges 3–14. The amplitude of the CFD fluctuations is comparable to the experiments. Gauge 3 shows higher pressure fluctuations than gauge 1. Dénos et al. [6] explained that unsteadiness is amplified along the front suction side due to the existence of an instantaneous convergent/divergent nozzle, enhancing the vane trailing-edge shock. A detailed analysis of the harmonic amplitudes shows that, at 50% of the span, the maximum for low and high occurs at gauge 3. At 15% span, the maximum occurs at gauge 4.

E. Unsteady Blade Force

The unsteady blade pressures are sources of tonal noise and unsteady forcing which may result in intolerable vibration levels and high cycle fatigue problems. The blade forces have been computed by integrating the measured time-resolved pressures on the blade. The maximum variations of rotor forces with respect to the mean level are 8.95% for the axial forces (at low) and 12.6% for the tangential forces (at nom).

Figure 12 displays the trajectory of the time-resolved force vector on the blade at midspan at nom-pressure ratio. Three different phases in the trajectory are identified. Between $\Phi_{\text{vane}} = -0.11$ and 0.0, the force experiences a maximum in the axial component, due to the effect of the vane left-running shock impacting in the blade crown. Secondly, from $\Phi_{\text{vane}} = 0.25$ to 0.5, the axial component of the blade

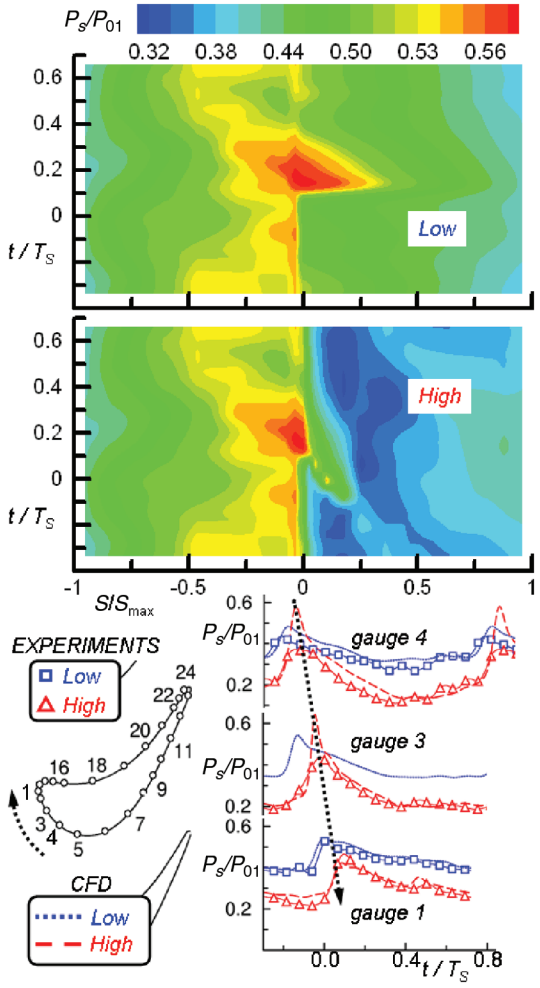

Fig. 11 Unsteady pressures on the rotor blade at 50% of span height at low- and high-pressure ratios.

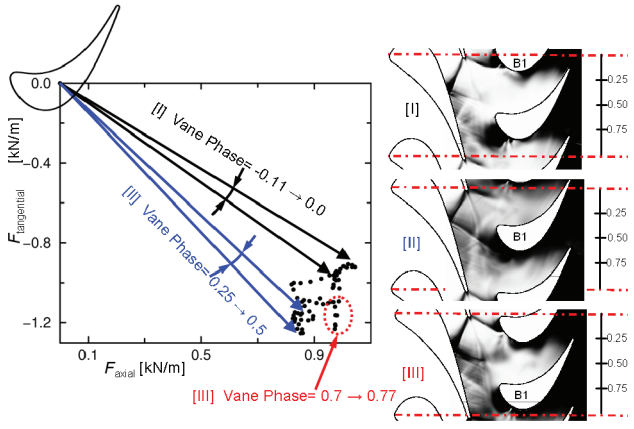

Fig. 12 Time-resolved blade force at midspan at nom-pressure ratio.

force remains nearly constant, because there is no shock impacting in the blade airfoil. At about phase 0.5, the reflected vane right-running shock strikes the blade, causing a net reduction in the axial force. Finally, between $\Phi_{vane} = 0.7$ and 0.77, the blade is submitted to a large variation in the tangential force, whereas the axial component is constant due to the impact of the reflected left-running vane shock.

F. Turbine Exit Flow

Figure 13 represents the radial distribution of the time-averaged Mach number, flow angle, and total temperature in plane 3. The 3-D Navier–Stokes solver predicts the experimental trend, with a small

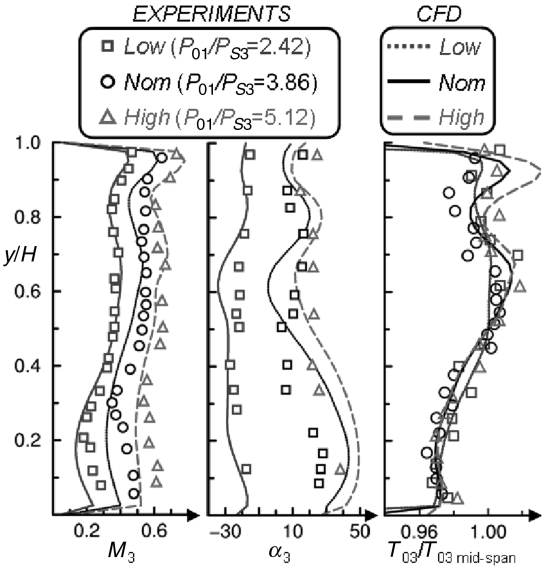

Fig. 13 Turbine exit radial distribution of absolute quantities: Mach number, flow angle, and total temperature.

underprediction of the total pressure in the hub region. By contrast, the CFD overpredicts the effect of the tip leakage jet on the temperature profile.

Figure 14 plots the time-averaged turbine exit total pressure as a function of the stator pitch for three different span heights: 15, 50, and 85%. Results are normalized by its mean value. The agreement between the experiments and the CFD is satisfactory. In the literature, these turbine exit pitchwise nonuniformities are attributed to the "vane wake avenues" or the vane secondary flows. At midspan, the minimum total pressure takes place at a vane pitch value ~0.5..

Figure 15 shows, in plane 2, the measured distribution of static pressure at 15% of the span, which is well matched with the CFD results (3-D RANS using the code of Arnone et al. [31]). P_{02} and P_{S2} were obtained numerically, then the absolute Mach number and the static temperature were computed:

$$M = \sqrt{\frac{2}{\gamma - 1}\left[\left(\frac{P_s}{P_0}\right)^{(1-\gamma)/\gamma} - 1\right]} \qquad T_s = T_0\left(\frac{P_s}{P_0}\right)^{(\gamma-1)/\gamma}$$

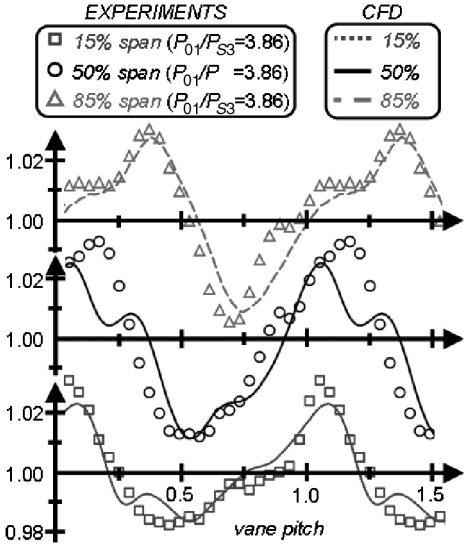

Fig. 14 Time-averaged total pressure in plane 3 at 15, 50. and 85% of span height (nom).

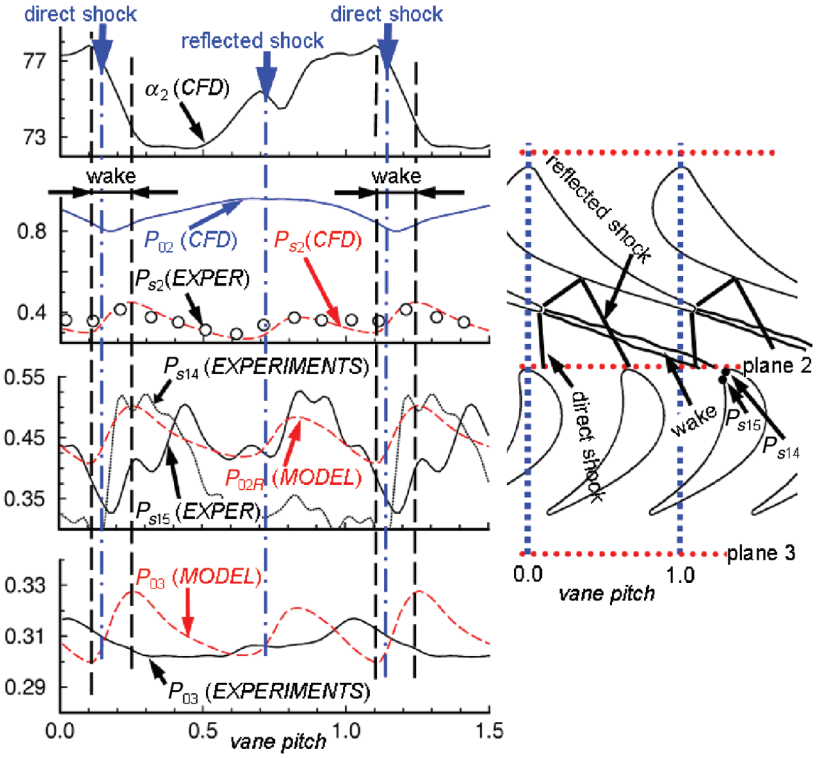

Fig. 15 Predicted time-averaged total pressure in plane 3 at 15% of span height.

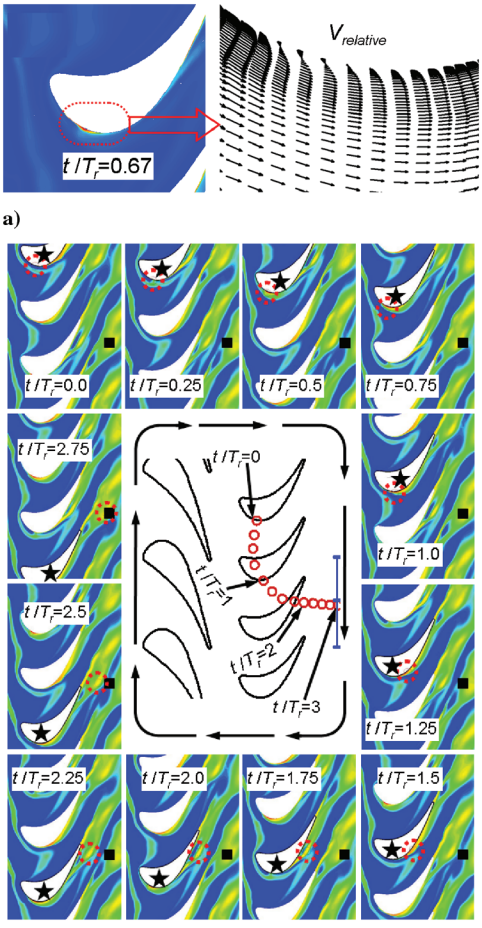

Fig. 16 Vortical bubble generation in the rotor: a) entropy field (left) and relative velocity field at $t/T_r = 0.67$; b) snapshots of entropy field at midspan in the absolute frame (black square corresponds to total pressure deficit zone). Center: schematic view of the convection of the vortical bubble.

Based on the Mach and static temperature, the vane exit velocity modulus can be computed along the pitch. Imposing the vane outlet flow angle obtained with the CFD, and knowing the rotor peripheral velocity, one can determine the rotor relative inlet velocity. Based on this velocity and the static temperature, it follows the rotor relative inlet total temperature is in the relative frame. Using this rotor relative inlet total temperature, the rotor inlet total pressure in the relative frame is computed P_{02R}. Interestingly, the predicted P_{02R} using the isentropic relationships have identical mean levels and features to the experimental data measured by a gauge mounted at the rotor leading edge. The rotor outlet conditions were computed applying conservation of rothalpy: $T_{03r} = T_{02r} - (u_2^2 - u_3^2)/2C_p$ and then $P_{03r} = P_{02r}(T_{03r}/T_{02r})^{\gamma/(\gamma-1)}$. Rigorously, this is an invalid assumption in unsteady flows. Nevertheless, the results of the model depict an excellent agreement between the predicted and measured P_{03}. The pitchwise shift between the prediction and the experimental data indicates that shock effects are not transported instantaneously downstream, but convected. This calculation helps to demonstrate that the main source of nonuniformities at the turbine exit are the vane exit shocks. Calculations assuming a constant P_{02} (without vane wakes) helped to isolate vane wake effects on the rotor upstream and downstream flowfield. The vane wake has a damping effect which attenuates the pressure gradients associated with the reflected shock. The change in the rpm implies a displacement in the pitchwise pressure deficit, nearly proportional to the rotational speed, proving that the effect is of a convective nature.

G. Vortical Bubble on the Rotor

The origins of the large pressure deficits downstream of the rotor were studied in detail by analyzing entropy contours. In the past, Johnson et al. [29] performed a detailed analysis of the schlieren flow visualization in a linear cascade using rotating bars. In that research, the passage of an NGV shock wave past the rotor leading edge gives rise to a small surface vortex, called a vortical bubble.

In the current investigation, the shock motion around the blade leading edge resulted in the creation of a separation bubble. Figure 16a displays the entropy field at $t/T_r = 0.67$ together with a zoom of the velocity field on the suction side at around $x/C_{ax} = 20\%$. A separated zone is clearly identified, characterized

by high entropy and reverse flow. Figure 16b represents different snapshots of the entropy flowfield at midspan in the absolute frame of reference, illustrating the vortical core movement generated by the shock impingement. The vortical structure is then convected along the suction side before it detaches completely from the rotor suction side. The center of Fig. 16b displays a schematic view of the convection of the entropy core along the rotor suction side. The displacement of the vortical bubble during three rotor passages is depicted by the successive circles. The vortical bubble appears on the suction side of the rotor at $t/T_r = 0.0$, it extends and is slightly convected upstream, as an effect of the shock. After the shock passage ($t/T_r = 0.75$), the entropy core begins its migration downstream, attached along the rotor suction side. At $t/T_r = 1.75$, the entropy core separates from the suction side at $x/C_{\text{ax}} = 70\%$ of chord. The location where the vortical structure detaches from the suction side corresponds to the location where the blade TE shock of the rotor impinges on the adjacent blade. Once the vortical core is shed from the rotor suction side, it is convected into the main stream, flowing into plane 3 exactly at a vane pitch value 0.5 after $t/T_r \sim 3$ where the deficit of total pressure is observed.

H. Turbine Efficiency

The turbine efficiency is measured using the mechanical method as described by Dénos et al. [32] and Yasa et al. [33]. Based on a careful uncertainty analysis, one can quote for a single experiment a random error of about 0.4%, whereas the systematic or bias error is around 1.9% for a single experiment. Please note that the repeatability in the efficiency is about 1%. The turbine efficiency is compared in Table 3 with the CFD predicted values. When the pressure ratio increases from low to nom, the experimental stage performance is reduced 4.9 points (the CFD underpredicts this drop to only 2.1 points). Because the mean vane exit velocity changes from 1.07 to 1.24, the shock losses are amplified. Moreover, the rotor positive incidence increases 4 deg from nom to low. The aerodynamic losses computed using the Kacker–Okapuu [34] correlation show a similar trend to the experiments, with a reduction amount of 4.4 points. Based on the loss's decomposition, one may conclude that turbine performance is mainly penalized due to the increased vane trailing-edge strength, although the change of incidence is responsible for only a 1% drop.

VI. Conclusions

Detailed experiments have been obtained on a highly loaded turbine stage at different pressure ratios, with a nominal reaction degree of 0.27 resulting in a supersonic vane outlet flow. Time-averaged and phase-resolved pressure and heat flux measurements have been achieved. Three-dimensional CFD have been performed to elucidate how the shock propagates across the stage. The NGV unsteady heat load is confined to the rear suction side, which is directly exposed to the highly unsteady interstage; the instantaneous heat transfer rates can double the time-averaged level. Static pressure and heat flux unsteadiness near the rotor leading edge rises with the pressure ratio. The increase of the fluctuations are a consequence of the more intense vane trailing-edge shocks, both direct and reflected striking the rotor. The strength, inclination, and curvature of the shock pattern depend not only on the pressure ratio, but on the blade height. The rotor blade is submitted to tangential force variations of about 32% of the mean level. The rotor disk forcing in the axial direction amounts to about 5% of the mean value. Based on the detailed analysis of the measurements, the vane direct and reflected shocks interactions with the rotor are explained.

Table 3 Turbine efficiencies measured and predicted by the CFD

η, %	Low	Nom	High
EXP	94.8	89.9	90.1
CFD	94.9	92.9	91.8

An important novelty of the present research is the identification of a vortical structure being generated on the rotor crown by the impingement of the vane TE shocks. This discrete vortex is then convected along the rotor suction side and is responsible for the large pressure deficit appearing downstream of the turbine. This is a novel finding, in contrast to the common belief in the literature that pressure deficits are due to vane wake avenues. The understanding of this mechanism should aid in the future redesign of more efficient turbines. The pressure loss generated by this vortical structure has been estimated using the vane exit flowfield and conservation of rothalpy.

Acknowledgments

Special thanks to B. Adiloglu, D. Delhaye, P. Palies, and G. Valentini for the experimental and CFD data processing. The authors would like to acknowledge the financial support of the European Commission and the European industrial manufacturers that participate in the Project TATEF2 (Turbine Aero-Thermal External Flows 2).

References

[1] Korakianitis, T.,"On the Prediction of Unsteady Forces on Gas Turbine Blades: Description of the Approach and Analysis of the Results," *Journal of Turbomachinery*, Vol. 114, Jan. 1992, pp. 114–131.

[2] Miller, R. J., Moss, R. W., Ainsworth, R. W., and Harvey, N. W., "Wake, Shock, and Potential Field Interactions in a 1.5 Stage Turbine, Part 1: Vane-Rotor and Rotor-Vane Interaction," American Society of Mechanical Engineers Paper 2002-GT-30435, 2002.

[3] Hilditch, M. A., Smith, G. C., Anderson, J. S., and Chana K. S., "Unsteady Measurements in an Axial Flow Turbine," *85th Propulsion and Energetic Panel Symposium*, AGARD CP No. 571, 1995.

[4] Giles, M. B., "Stator-Rotor Interaction in a Transonic Turbine," *Journal of Propulsion and Power*, Vol. 6, No. 5, 1990, pp. 621–627.

[5] Laumert, B., Martensson, H., and Fransson, T., "Investigation of Unsteady Aerodynamic Blade Excitation Mechanisms in a Transonic Turbine Stage, Part 1: Phenomenological Identification and Classification: Analytical Description and Quantification," *Journal of Turbomachinery*, Vol. 124, No. 3, 2002, pp. 410–428. doi:10.1115/1.1458577

[6] Dénos, R., Arts, T., Paniagua, G., Michelassi, G., and Martelli, F., "Investigation of the Unsteady Rotor Aerodynamics in a Transonic Turbine Stage," *Journal of Turbomachinery*, Vol. 123, No. 1, Jan. 2001, pp. 81–89. doi:10.1115/1.1314607

[7] Graham C. G., and Kost, F. H., "Shock Boundary Layer Interaction on High Turning Transonic Turbine Cascades," American Society of Mechanical Engineers Paper 79-GT-37, 1979.

[8] Johnson, A. B., Rigby, M. J., Oldfield, M. L., Ainsworth, R. W., and Oliver, M. J., "Surface Heat Transfer Fluctuations on a Turbine Rotor Blade Due to Upstream Shock Wave Passing," American Society of Mechanical Engineers Paper 88-GT-172, 1988.

[9] Johnson, A. B., Rigby, M. J., and Oldfield, M. L. G., "Unsteady Aerodynamic Phenomena in a Simulated Wake and Shock Wave Passing Experiment," AGARD Paper CP-468, 1989.

[10] Dunn, M. G., Bennett W. A., Delaney, R. A., and Rao, K. V., "Investigation of Unsteady Flow Through a Transonic Turbine Stage: Comparison for Time-Averaged and Phase-Resolved Pressure Data," AIAA Paper 90-2409, 1990.

[11] Abhari, R. S., Guenette, G. R., Epstein, A. H., and Giles, M. B., "Comparison of Time-Resolved Turbine Rotor Blade Heat Transfer Measurements and Numerical Calculations," American Society of Mechanical Engineers Paper 91-GT-268, 1991.

[12] Popp, O., Smith, D., Bubb, J., Grabowski, H., and Diller, T., "Steady and Unsteady Heat Transfer in a Transonic Film Cooled Turbine Cascade," American Society of Mechanical Engineers Paper 99-GT259, 1999.

[13] Nix, A. C., Reid, T., Peabody, H., Ng, W. F., Diller, T. E., and Schetz, J. A., "Effects of Shock Wave Passing on Turbine Blade Heat Transfer in a Transonic Cascade," AIAA Paper 97-0160 1997.

[14] Nix, A., Smith A., and Diller T., "Unsteady Effect of Passing Shocks on Pressure Surface Versus Suction Heat Transfer in Film-Cooled Turbine Blades," American Society of Mechanical Engineers Paper GT2003-38530, 2003.

[15] Rao, K. V., and Delaney R. A., "Investigation of Unsteady Flow Through Transonic Turbine Stage," AIAA Paper 90-2408, 1990.

[16] Saxer, A., and Felici, H., "Numerical Analysis of Three-Dimensional Hot Streak Migration and Shock Interaction in a Turbine Stage," *Journal of Turbomachinery*, Vol. 118, April 1996, pp. 268–277.
[17] Sieverding, C. H., Arts, T., Dénos, R., and Martelli, F., "Investigation of the Flowfield Downstream of a Turbine Trailing Edge Cooled Nozzle Guide Vane," *Journal of Turbomachinery*, Vol. 118, April 1996, pp. 291–300.
[18] Yasa, T., Paniagua, G., and Dénos, R., "Application of Hot-Wire Anemometry in a Blow-Down Turbine Facility," *Journal of Engineering for Gas Turbines and Power*, Vol. 129, No. 2, 2007, pp. 420–427. doi:10.1115/1.2364191
[19] Sieverding, C. H., and Arts, T., "VKI Compression Tube Annular Cascade Facility CT3," American Society of Mechanical Engineers Paper 92-GT-336, 1992.
[20] Dénos, R., and Paniagua, G., "Effect of Vane-Rotor Interaction on the Unsteady Flow Field Downstream of a Transonic HP Turbine," *Proceedings of the Institution of Mechanical Engineers, Part A: Journal of Power and Energy*, Vol. 219, No. 6, 2005 pp. 431–442. doi:10.1243/095765005X31180
[21] Billiard, N., Iliopoulou, V., Ferrara, F., and Dénos, R., "Data Reduction and Thermal Product Calibration for Single and Multi-Layered Substrates Thin Film Gauges," *Proceedings of the 16th Symposium on Measuring Techniques in Transonic and Supersonic Flow in Cascades and Turbomachines*, von Kármán Inst. RP 2002-47, 2002.
[22] Dénos, R., "Influence of Temperature Transients and Centrifugal Force on Fast Response Pressure Transducers," *Experiments in Fluids*, Vol. 33, 2002, pp. 256–264.
[23] Cambier, L., and Gazaix, M., "elsA: An Efficient Object-Oriented Solution to CFD Complexity," *Proceedings of the 40th AIAA Aerospace Science Meeting & Exhibit*, AIAA 2002-0108, 2002.
[24] Menter, F., "Improved Two-Equation k-ω Turbulence Models for Aerodynamic Flows," Technical Rept. NASA, TM 103975, 1992.
[25] Arnal, D., Habiballah, M., and Coustols, E., "Théorie de l'Instabilité Laminaire et Critères de Transition en Écoulement bi et Tridimensionnel," La Recherche Aérospatiale No. 2, 1984.
[26] Erdos, J. L., and Alzner, E., "Computation of Unsteady Transonic Flows Through Rotating and Stationary Cascades," NASA CR-2900, 1977.
[27] Billonnet, G., Plot, S., and Leroy, G., "Implementation of the elsA Software for the Industrial Needs of Flow Computations in Centrifugal Compressors," *41ème Colloque d'Aérodynamique Appliquée*, Assoc. Aeronautique et Astronautique de France, Paris, 2006.
[28] Toussaint, C., "Mise en Oeuvre des Propriétés de Déphasage Spatio-Temporel pour le Calcul Instationnaire d'étage de Turbomachine," RT ONERA NRT47/01025DAAP, July 2000.
[29] Johnson, A. B., Oldfield, M. L. G., Rigby, M. J., and Giles, M. B., "Nozzle Guide Vane Shock Wave Propagation and Bifurcation in a Transonic Turbine Rotor," American Society of Mechanical Engineers Paper 90-GT-310, 1990.
[30] Paniagua, G., Dénos, R., and Almeida, S., "Effect of Hub Endwall Cavity Flow Ejection on the Flowfield of a Transonic High Pressure Turbine,". *Journal of Turbomachinery*, Vol. 126, No. 4, Oct. 2004, pp. 578–586. doi:10.1115/1.1791644
[31] Arnone, A., Liou, M.-S., and Povinelli, L., "Multigrid Calculation of Three-Dimensional Viscous Cascade Flows," *Journal of Propulsion and Power*, Vol. 9, No. 4, 1993, pp. 605–614.
[32] Dénos, R., Paniagua, G., Yasa, T., and Fortugno, E., "Determination of the Efficiency of a Cooled HP Turbine in a Blowdown Facility," American Society of Mechanical Engineers Paper GT2006-9046, 2006.
[33] Yasa, T., Paniagua, G., and Bussolin A., "Performance Analysis of a Transonic High Pressure Turbine," *Proceedings of the Institution of Mechanical Engineers, Part A: Journal of Power and Energy*, Vol. 221, No. 6, Sept. 2007, pp. 769–778. doi:10.1243/09576509JPE467
[34] Okapuu, U., "Some Results from Tests on a High Work Axial Gas Generator Turbine," American Society of Mechanical Engineers Paper 74-GT-81, 1974.

C. Tan
Associate Editor